Spectroscopic confirmation and modelling of two lensed quadruple quasars in the Dark Energy Survey public footprint

C. Spiniello [1,2]★ A. V. Sergeyev,[3,4] L. Marchetti [5,6,7] C. Tortora,[8]
N. R. Napolitano,[1,9] V. Shalyapin,[10,11] A. Agnello,[12] F. I. Getman,[1] M. Vaccari [6,7]
S. Serjeant,[13] L. V. E. Koopmans,[14] A. J. Baker,[15] T. H. Jarrett,[5] G. Covone[16,17] and
G. Vernardos [14]

Affiliations are listed at the end of the paper

ABSTRACT

Quadruply lensed quasars are extremely rare objects, but incredibly powerful cosmological tools. Only few dozen are known in the whole sky. Here we present the spectroscopic confirmation of two new quadruplets WG0214-2105 and WG2100-4452 discovered by Agnello & Spiniello (2018) within the Dark Energy Survey public footprints. We have conducted spectroscopic follow-up of these systems with the Southern African Large Telescope as part of a program that aims at confirming the largest possible number of strong gravitational lenses in the equatorial and Southern hemisphere. For both systems, we present the sources spectra that allowed us to estimate their redshifts and unambiguously confirm their lensing nature. For the brighter deflector (WG2100-4452) we measure the spectroscopic redshift and the stellar velocity dispersion from optical absorption lines in the spectrum. For the other system we infer the lens redshift from photometry, being the quality of the spectra not good enough. We obtain photometry for both lenses, directly from multiband images, isolating the lenses from the quasars. One of the quadruplets, WG0214-2105, was also observed by Pan-STARRS, allowing us to estimate the apparent brightness of each quasar image at two different epochs, and thus to find evidence for flux variability. This result could suggest a microlensing event for the faintest components, although intrinsic variability cannot be excluded with only two epochs. Finally, we present simple lens models for both quadruplets, obtaining Einstein radii, singular isothermal ellipsoid velocity dispersions, ellipticities, and position angles of the lenses, as well as time-delay predictions assuming a concordance cosmological model.

Key words: gravitational lensing: strong – techniques: spectroscopic – surveys – galaxies: formation.

1 INTRODUCTION

According to the estimate of Oguri & Marshall (2010), quadruplets represent ∼14 per cent of a statistically complete sample of lensed quasars. The quadruplet configuration, in fact, requires a closer alignment between the source and the deflector than the one needed for the more common doublet configuration.[1] However, when the

number of source images is doubled, the information that can be gathered in terms of stellar mass fraction and deflector potential is larger (e.g. Schechter & Wambsganss 2004; Treu & Marshall 2016). Quadruplets have also been shown to be valuable cosmological tools (Refsdal 1964; Blandford & Narayan 1992; Witt, Mao & Keeton 2000; Suyu et al. 2013; Treu & Marshall 2016; Bonvin et al. 2017) and useful for microlensing studies to investigate the inner parts of quasar accretion discs (Schechter & Wambsganss 2002; Kochanek 2004; Eigenbrod et al. 2008; Blackburne et al. 2011; Mediavilla et al. 2017; Vernardos 2018). For instance, studies based on blind analysis have shown that a single quadruplet can be used to measure the so-called time-delay distance ($D_{\Delta t}$), a multiplicative combination of the three angular diameter distances between the

---

★ E-mail: chiara.spiniello@gmail.com, chiara.spiniello@inaf.it
[1]We note however that the magnification bias (Turner 1980), due to the fact that multiple imaging magnifies the source, is larger in the case of a quadruplet configuration, compensating, at least partially, for the smaller cross-section.

observer, deflector, and source,[2] with an uncertainty of 5–7 per cent (Suyu et al. 2012). Since $D_{\Delta t}$ is inversely proportional to the Hubble constant, H_0 (Linder 2011; Suyu et al. 2012), and more weakly dependent on other cosmological parameters, obtaining a precise estimation of it through time-delay lenses allows one to break some of the main degeneracies in the interpretation of cosmic microwave background data. Moreover, time-delay distances are independent of the local distance ladder and give comparable precision on H_0, providing a crucial test of potential systematic uncertainties.[3]

In this paper, we report the spectroscopic confirmation of two recently discovered quadruplets: WG0214-2105 and WG2100-4452, both identified in the Dark Energy Survey (DES; Abbott et al. 2018) DR1 public footprints, using the source-based methods developed and presented in Agnello & Spiniello (2018, hereafter A18) to find lens candidates in wide-sky photometric multiband surveys. The spectroscopic confirmation has been carried out using the Southern African Large Telescope (SALT; Buckley, Swart & Meiring 2006) as part of the observing programme *Gotta catch'em all* (2018-2-SCI-020, PI: Marchetti).

The paper is organized as follow. In Section 2, we give details on the SALT observing programme and the selected candidates. A brief description of the two new quadruplets, including their coordinates and infrared magnitudes used at the pre-selection stage, is provided in Section 3. In Section 4, we report the results of a photometric analysis, which then leads to a preliminary variability analysis for one of the systems. In Section 5, we present the obtained SALT spectra for both systems, and highlight the redshift determinations for the sources and the deflectors. In Section 6, we provide simple lensing models for both quadruplets. We summarize our findings and conclude in Section 7.

Throughout the paper, we adopt a flat Λ cold dark matter cosmology with $\Omega_M = 0.3$, $\Omega_\Lambda = 0.7$, and $H_0 = 70\ \mathrm{km\,s^{-1}\,Mpc^{-1}}$.

2 THE SALT OBSERVING PROGRAMME

Our observing programme: '*Gotta catch'em All*, the spectroscopic follow-up of strong gravitational lenses from KiDS and KABS surveys' (PI: L. Marchetti, ID: 2018-2-SCI-020) has the goal of spectroscopically confirming optically selected strong gravitational lens (SL) candidates, both quasi-stellar object (QSO)–galaxy, and galaxy–galaxy (gravitational arcs) systems. The candidates have been found by exploiting the improved image quality and the more extended and homogeneous sky coverage achieved with new, deep optical surveys. In particular, we focus on the Kilo Degree Survey (KiDS; de Jong et al. 2015, 2017), because of its depth, exquisite image quality and quite stringent seeing constraints [limiting magnitude of 25 at 5σ in 2 arcsec aperture and mean full width at half-maximum (FWHM) of 0.7 arcsec in r band], and on the KiDS VST-ATLAS Bridging Survey (KABS; Getman et al. in preparation),[4] which images a previously almost uncovered region of the southern sky. Finally, we also include a few very promising

candidates from the DES public footprint, which were recently found by our team (Agnello & Spiniello 2018).

After almost 2 yr, we have collected a list of ∼300 high-grade candidates which need spectroscopic confirmation and redshift measurements to translate our lens model results (e.g. Einstein radii) into physical mass measurements. We have already presented the search methods as well as the KiDS candidates in recently published papers (Petrillo et al. 2017, 2019; Spiniello et al. 2018, hereafter S18), and we will present the KABS candidates in a paper in preparation (Spiniello et al. in prep).

Full results from the first semester of SALT observations, still on-going, will be presented in a dedicated, future, paper (Marchetti et al. in prep). In this paper, we focus on the DES candidates: two quadruply lensed QSOs for which the spectroscopic confirmation was the last required step to unambiguously confirm their lensing nature. These pilot observations have been carried out to test our strategy and integration times before proceeding with a larger candidate list (arcs and QSOs) from the KIDS and KABS surveys.

3 TWO NEW QUADRUPLETS IN THE SOUTHERN HEMISPHERE: WG0214-2105 AND WG2100-4452

Agnello (2018, hereafter ARN18) reported the discovery of WG0214-2105 (RAJ2000: 02:14:16.37, DECJ2000: -21:05:35.3), which was found by cross-matching the publicly available data of three wide-area sky surveys in the Southern hemisphere (DES DR1, Abbott et al. 2018; VST-ATLAS, Shanks et al. 2015; and Pan-STARRS, Chambers et al. 2016). The multiple images, in the typical fold/cross configurations, are characterized by 'white' optical colours, 'blue' mid-IR colours and high UV deficit (ARN18).

The discovery of WG2100-4452 (RA J2000: 21:00:14.9, Dec. J2000: −44:52:06.4) has been reported in A18, where we exploit several complementary methods to search for lensed quasars in wide-area photometric surveys. In particular, this previously unknown quadruplet in the DES footprint has been found by pre-selecting QSO-like objects based on infrared colours (from the Wide-Infrared Survey Explorer, WISE; Wright et al. 2010) and then making use of the high spatial resolution of the Gaia Mission (Gaia Collaboration 2016; Lindegren et al. 2016) to identify single WISE objects with multiple Gaia matches. We refer the reader to A18 for a more comprehensive description of this and the other methods, and for a complete list of other similarly identified lens candidates.

Both WG0214-2105 and WG2100-4452 have also been shown to be easily compatible with simple lens models (Wynne & Schechter 2018).

In this paper we present their spectroscopic confirmation, with estimation of the source and deflector redshifts, as well as *griz*-photometry obtained directly from the DES images and lensing modelling. We note that a very recent paper, contemporary to this work, has been published by Lee (2019), reporting a spectroscopic confirmation of WG0214-2105 with Gemini Multi-Object Spectrographs. Here we provide a more detailed analysis of the spectral, photometric, and lensing properties of the latter system, comparing our inferences for the source and deflector redshifts with the related findings in Lee (2019).

Table 1 reports, for the two lens systems, coordinates and WISE

---

[2] $D_{\Delta t} = (1 + z_l)[D_l D_s / D_{ls}]$, with z_l the redshift of the deflector, D_l the angular diameter distance of the lens from the observer, D_s the distance of the source from the observer, and D_{ls} the relative distance between the lens and the source.

[3] See e.g. the work done by the H_0 Lenses in COSMOGRAIL's Well-spring (H0LiCOW, https://shsuyu.github.io/H0LiCOW/site/) Collaboration, of which some of the authors of this publication are members.

[4] KABS is a new Guarantee Time Observation program (PI N. R. Napolitano) at the VLT Survey Telescope (VST; Capaccioli & Schipani 2011), which

is equipped with the wide field camera OmegaCAM Kuijken (2011) and operating at the ESO observatory in Cerro Paranal (Chile).

Table 1. Coordinates, infrared magnitudes from the WISE catalogue (Wright et al. 2010), converted in AB system and spectroscopic observations settings for the two quadruplets. For WG0214-2105 we obtained two different observation blocks, with two different position angle orientations ($-35°$ and $+50°$, respectively), as indicated in the table.

ID	RA (J2000)	Dec. (J2000)	W1 (mag)	W2 (mag)	W3 (mag)	W4 (mag)	Total exp. time (s)	Slit width (arcsec)	PA (°)
WG0214-2105	02:14:16.4	$-21:05:35.3$	17.79 ± 0.03	17.99 ± 0.06	17.0 ± 0.2	15.2 ± 0.3	1800	2.0	$-35/+50$
WG2100-4452	21:00:14.9	$-44:52:06.4$	16.82 ± 0.03	16.74 ± 0.03	15.9 ± 0.1	14.8 ± 0.3	1500	3.0	$+40$

infrared magnitudes, used for pre-selection and converted from their native Vega system to AB, to better compare them with the optical ones given in the latter system throughout this paper. We also give details about the observational blocks (slit position, orientation, and integration times) that we will present in detail in Section 5.

4 ACCURATE ASTROMETRY AND PSF PHOTOMETRY ANALYSIS

Following the recipe detailed in S18, we performed direct image analysis (DIA) on the multiband DES images of the two systems. Briefly, we simultaneously fitted a point-PSF (point spread function) model to all the QSO multiple images in each of the single-band cut-outs, for *griz* bands, and then generated subtracted images that we visually inspected to identify the position of the deflector. Accurate astrometry is, in fact, of great help when extracting the 1D spectra from the long-slit data and it is also very useful when performing lensing and mass modelling.

We then derived, for each band, photometry on all the components (A = brightest QSO image, D = faintest QSO image, G = lens galaxy) using the code GALFIT (Peng et al. 2002). We calculated the PSF from a nearby star, to minimize the effect of distortion on the field and then modelled each quasar image simultaneously with a point-like PSF profile and the galaxy with a Sérsic profile convolved with the PSF. Specifically, we assumed a de Vaucouleurs profile using a fixed Sérsic index[5] $n = 4$, to model the light distribution of the lens galaxy.

Fig. 1 shows the results of the PSF fitting. For WG0214-2105, we also performed DIA on the Pan-STARRS images. In each line of the figure, the left-most panel shows the *griz*-combined colour cut-outs of 10 arcsec × 10 arcsec size, and the middle panel shows the same image after the 4 QSO components have been subtracted, and from which it is possible to identify the presence of the deflector. Finally, the right-most panel shows the residuals after fitting and subtracting also the light of the lens galaxy. Table 2 reports the relative positions of all the QSO components obtained from the *r*-band DES images, as well as the inferred magnitudes for *g*, *r*, *i*, and *z* bands with their uncertainties, as calculated by GALFIT.

4.1 Variability evidence for WG0214

Quasar microlensing occurs when the light of the source, already deflected by the lens gravitational field, is also affected by the gravitational field of relatively low-mass ($10^{-6} < m/M_\odot < 10^3$) bodies moving along the line of sight (e.g. single stars, brown dwarfs, planets, globular clusters, etc.). More specifically, microlensing is observed when the angular size of such bodies is smaller than the Einstein radius (θ) of the lensing system and therefore comparable

with quasar angular size. Thus, microlensing is a very useful tool to constrain quasar structure as well to estimate the masses of these compact bodies (Kochanek 2004).

During a microlensing event, the mass of the micro-deflector is not large enough to cause a measurable displacement of the light path, but, due to the relative motion between the source quasars, the lenses and the observer, a change in the magnification with time can be detected (Schmidt & Wambsganss 2010). Thus, the apparent brightness of the source can change by more than a magnitude on time scales of weeks to months or years.[6] Unlike the intrinsic quasar variability, however, microlensing variability is uncorrelated between images.

Microlensing has a number of very important astrophysical applications. In particular, it can help in determining the existence and effects of compact objects along the line of sight, in studying in great detail the size, structure, and light distribution of the source quasars (Dai et al. 2010; Morgan et al. 2010; O'Dowd et al. 2015) and in constraining the masses and mass distributions of lensing objects and their environments (e.g. Cowley et al. 2017).

For WG0214-2105, we can compare two magnitude measurements obtained from multiband images taken at different epochs: DES, taken in 2016, and Pan-STARRS, taken in 2014. Although with only two measurements one cannot build a detailed light curve, these data allowed us to detect time variation of the flux of each quasar component, which appears to be uncorrelated with wavelength and thus suggestive of a microlensing origin. Fig. 2 plots the magnitudes calculated for different filter bands (*g*, *r*, *i*) from Pan-STARRS (upper panel) and DES (lower panel) for the four QSO images of WG0214-2105. We excluded the *z*-band image because it was very noisy for the Pan-STARRS case. The brightness of the B, C, and D components changes with time, without any clear correlation between wavelength and magnitude. This result seems to indicate a microlensing effect, although we stress that chromatic variability cannot be entirely excluded based on just two epochs of broad-band imaging. Another argument in favour of microlensing comes from Palanque-Delabrouille et al. (2011) and in particular from their Fig. 5, which shows the variability structure function for a typical quasar (the change in amplitude as a function of time between observations at different epochs). The function predicts that a change of $\sim 0.3 - 0.5$ mag, similar to what we observe for the D component, is expected only if the two epochs are separated by several years.[7] We caution the reader, however, that delay among different light-curves might cause a large flux variation, as shown in Courbin et al. (2018) for the lens D0408. Flux ratio variations among light-curves also have implications for claims of substructure detection, as was shown explicitly by Agnello et al. (2017) on the same lens.

---

[5]We note that more detailed modelling, letting for instance the Sérsic index varying as free parameter, is not ideal since the images are too noisy.

[6]The first detection of a microlensing event from photometric variations was reported in Irwin et al. (1989), for the Q2237+0305 lens system.

[7]We note that optically violent variable quasars can vary at this level on time-scales of days; however these systems are extremely rare.

WG0214-2105
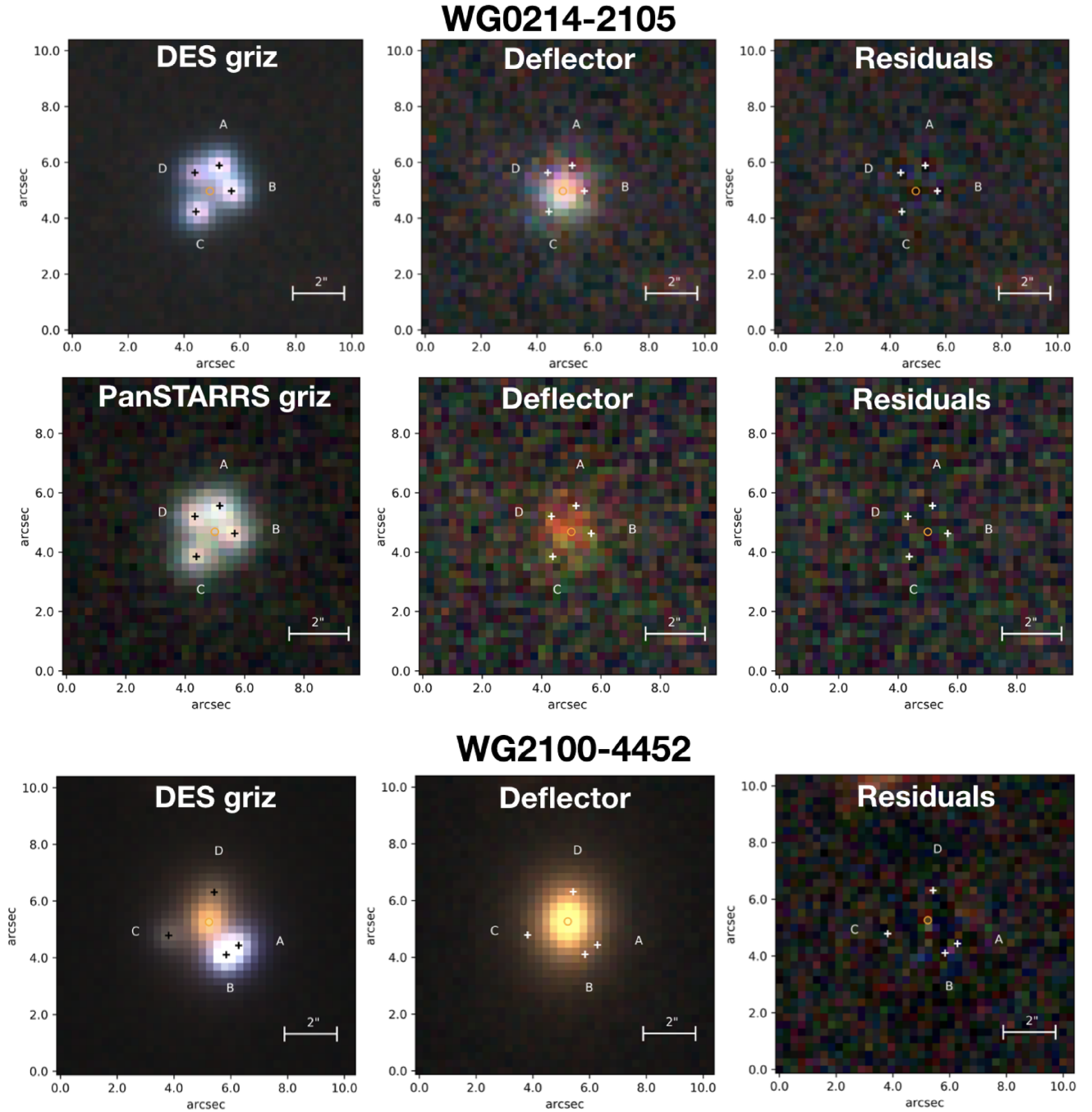
WG2100-4452

Figure 1. Cut-outs generated combining *g*-, *r*-, *i*- and *z*-band DES images (upper panels) and Pan-STARRS images (middle panels) for WG0214-2105, and for WG2100-4452, observed only from DES (lower panels). For each system, we show the original cut-out (left-hand column), the result after subtracting the multiple QSO images (middle column), and the residuals obtained after also subtracting the deflector (right-hand column).

5 SALT SPECTROSCOPIC FOLLOW-UP

In 2018 November, we obtained long-slit spectroscopy for the two quadruplets with the Robert Stobie Spectrograph (RSS) instrument and the PG0900 grating (grating-angle = 15.875), covering from 4490 to 7540 Å with resolution $R = 1000$ measured from the OI5577 sky line, and using a 2×4 binning, corresponding to ∼0.5 arcsec pix^{-1} in the spatial direction and to 0.97Å pix^{-1} in the dispersion direction.

As already highlighted, these two DES systems, being bright and visible at the beginning of the SALT observation semester, have

been used as 'test-cases' in modest observing condition (seeing > 1.5 arcsec) and non-optimal observing time (twilight), mainly to test our choices of grating, spatial binning and integration time on target.

The data were reduced with two independent methods, namely the SALT science pipeline (PYSALT; Crawford et al. 2010)[8] and standard IRAF routines. One-dimensional (1D) spectra were extracted and analysed with custom IDL and MATHEMATICA codes. In the following

[8] http://pysalt.salt.ac.za/

Table 2. Astrometric and photometric properties of all components of the two systems. Relative positions are computed from the *r*-band DES images and always use as reference the brightest QSO image (A). Magnitudes in the *griz* bands have been computed using GALFIT and are given in the AB system.

ID	Comp.	δx (*r* band, arcsec)	δy (*r* band, arcsec)	*g* (mag)	*r* (mag)	*i* (mag)	*z* (mag)
WG0214-2105	A	$+0.000 \pm 0.005$	0.000 ± 0.003	20.47 ± 0.04	20.30 ± 0.02	20.33 ± 0.02	20.14 ± 0.02
WG0214-2105	B	$+0.460 \pm 0.003$	-0.915 ± 0.003	20.39 ± 0.03	20.26 ± 0.02	20.26 ± 0.02	20.07 ± 0.03
WG0214-2105	C	-0.852 ± 0.003	-1.678 ± 0.003	20.50 ± 0.04	20.44 ± 0.04	20.34 ± 0.02	20.18 ± 0.02
WG0214-2105	D	-0.876 ± 0.008	-0.234 ± 0.005	21.11 ± 0.06	20.83 ± 0.03	20.71 ± 0.03	20.61 ± 0.03
WG0214-2105	G	-0.34 ± 0.05	-0.96 ± 0.05	20.83 ± 0.15	20.00 ± 0.07	19.46 ± 0.04	19.37 ± 0.06
WG2100-4452	A	$+0.000 \pm 0.011$	0.000 ± 0.008	19.91 ± 0.05	19.85 ± 0.05	19.58 ± 0.10	19.64 ± 0.06
WG2100-4452	B	-0.437 ± 0.005	-0.332 ± 0.005	19.23 ± 0.02	19.12 ± 0.02	18.99 ± 0.05	18.84 ± 0.02
WG2100-4452	C	-2.48 ± 0.01	0.36 ± 0.01	21.10 ± 0.01	21.07 ± 0.02	20.82 ± 0.04	20.70 ± 0.04
WG2100-4452	D	-0.86 ± 0.02	1.90 ± 0.02	21.70 ± 0.03	21.52 ± 0.05	21.31 ± 0.08	21.20 ± 0.06
WG2100-4452	G	-1.039 ± 0.003	0.823 ± 0.005	18.81 ± 0.01	17.68 ± 0.01	17.30 ± 0.01	16.83 ± 0.04
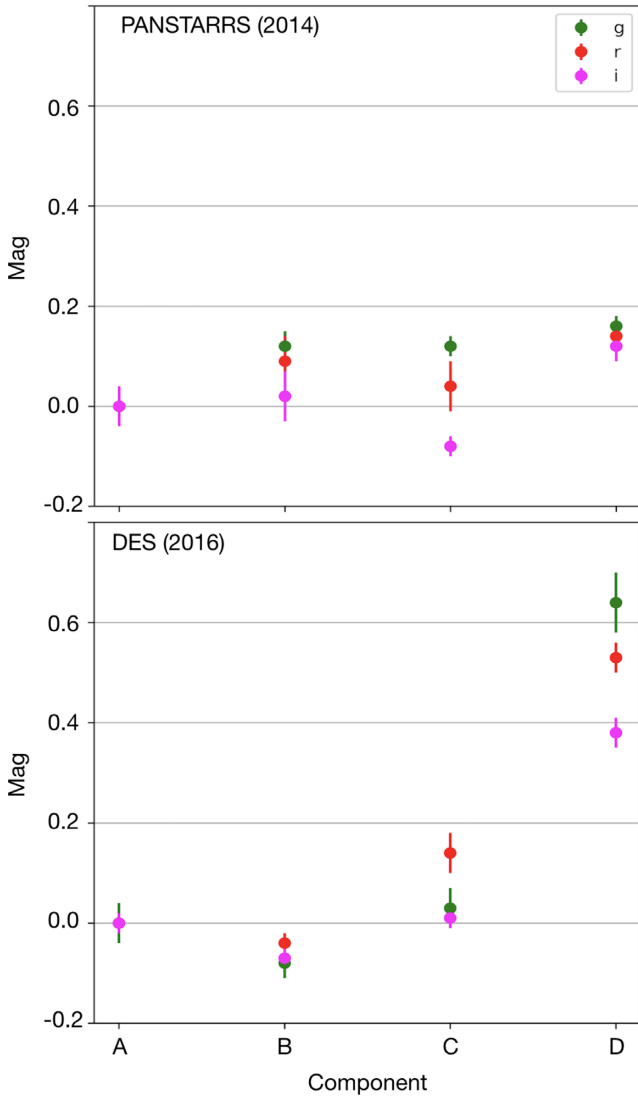
Figure 2. Estimated magnitudes at different filter bands (*g*, *r*, *i*) from Pan-STARRS images taken in 2014 (upper panel) and from DES images taken in 2016 (lower panel) for the four QSO images of WG0214-2105. The brightness of the B and the D components changes with time, without a clear correlation with wavelength. This result could indicate the presence of microlensing.

Table 3. Inferred redshifts for the lenses and the sources. The (p) indicates that the redshift estimate has been inferred with photometry, while the (s) indicates that the redshift estimate comes from identification of spectral lines.

| Name	z_l	z_s
WG0214-2105	0.22 ± 0.09 (p)	3.229 ± 0.004 (s)
WG0214-2105	0.53 ± 0.08 (p)	3.229 ± 0.004 (s)
WG2100-4452	0.203 ± 0.002 (s)	0.920 ± 0.002 (s)

section we discuss the extraction of the spectra, de-blending of the components and estimation of the redshift for each target separately. The redshifts are reported in Table 3.

5.1 WG0214-2105

We observed WG0214-2105 in two separate observing blocks with a slit of 1.5 arcsec × 8 arcsec and two different position angles (PA): $-35°$ (PA-35 configuration) and $+50°$ (PA$+50$ configuration). Both observations were centred on the deflector, and both integrated for 1800 seconds on target. Seeing was not ideal (≈ 1.8 arcsec) but the night was clear. These configurations were motivated by the need to maximize the exposure time on the faint lens galaxy, and simultaneously obtain at least two completely independent spectra of the QSO components (A+B+D from PA-35 and A+C from PA$+50$).

The extracted spectra for the two position angles are shown in the upper panel of Fig. 3, where we label the main quasar emission lines (Ly α, Si IV, O IV], He II, O III]) that allowed a secure determination of the redshift of the source ($z_s = 3.229 \pm 0.004$). This value is in good agreement (within 2σ error) with the value of $z_s = 3.242 \pm 0.005$ reported in Lee (2019).

Unfortunately the quality of the long-slit spectra and the high contamination by the quasar did not allow us to securely determine the redshift of the deflector (z_l), although we identified some absorption lines (corresponding to more than one redshift, and therefore indicating the presence of galaxies along the line of sight). Therefore we infer z_l from photometry. To estimate the photometric redshift of the deflector we compared its PSF colours as derived in Section 4 with galaxy spectra from the Sloan Digital Sky Survey (SDSS, DR14, Abolfathi et al. 2018). In particular, we select all galaxies in SpecPhotoAll with magnitudes within 2σ of those obtained from our photometry (we use the petroMag and its petroMagErr for each band) of the lens, and retain their spectroscopic redshifts. The resulting histogram, plotted in
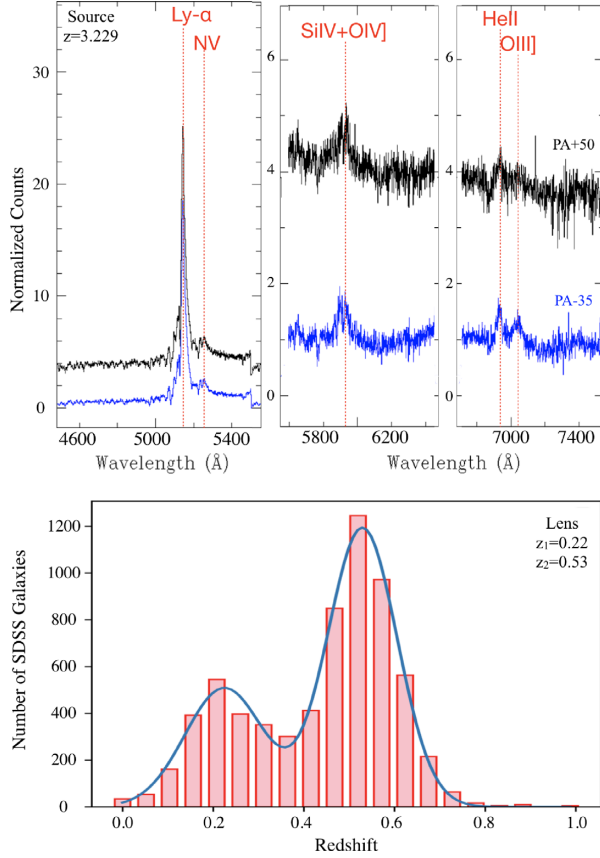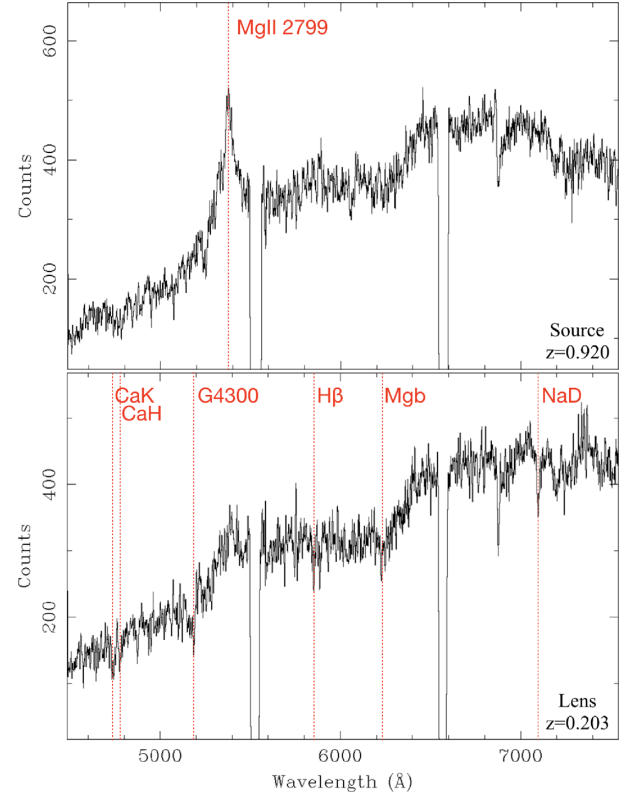
Figure 3. SALT spectra of the lensed quasar (upper panels) and redshift distribution of the deflector (lower panel) for WG0214-2105. For the source, we show the two independent spectra extracted from the two slits with different position angles, corresponding to the A+C components (PA+50, black) and the A+B+D components (PA−35, blue). We zoom-in on the most prominent emission lines (Ly α in the left-hand panel, Si IV+O IV] in the middle panel and He II and O III] in the right-hand panel) that allowed us to securely infer its redshift. Unfortunately, the spectrum of the deflector did not allow us to do the same and therefore we used the photometric results to infer its redshift. We plot here the histogram of the spectroscopic redshifts from SDSS-DR14 `SpecPhotoAll` galaxies with similar Petrosian magnitudes (within 2σ uncertainties).

the lower panel of Fig. 3, is double peaked. We then calculated the mean and standard deviation of the both peaks, fitting two normal distributions: $z_{l1,WG0214} = 0.22 \pm 0.09$, $z_{l2,WG0214} = 0.53 \pm 0.08$. We note that the second peak (higher) of the histogram is consistent with the tentative redshift reported in Lee (2019).

5.2 WG2100-4452

For WG2100-4452 we obtained only one slit position with PA = $40°$ and width = 3.0 arcsec, observed under thin cloud and very high lunar brightness (94 per cent, corresponding to a moon distance of $30°$). Unfortunately, with such a configuration, all four images of the QSO are blended in the slit; it is therefore impossible to properly separate the components, especially for the two brightest ones. For the dim C and D components, unfortunately the short integration time that we obtained (1200 s) did not allow us to identify their signal. However, having clear evidence for emission lines from A+B, given the very specific geometrical configuration and the colours, and finally, given that this system can be perfectly fit with


Figure 4. SALT spectra of the lensed quasar (upper panel) and the deflector (lower panel) of WG2100-4452 smoothed with a boxcar of 5 pixels for better visualization. We securely infer the redshift for both the source and the deflector, thanks to the identification of emission and absorption lines, marked in the figure with vertical lines. De-blending the multiple images of the QSO is unfortunately not possible with the current slit configuration.

a simple lens model (as we will show in Section 6), we are fully confident about its lensing nature.

The accurate astrometric information provided by our analysis helped us to decompose the two-dimensional (2D) spectrum, separating, at least partially, the lens from the source. To this end, we considered a two-component model, with the A+B QSO being the first and the deflector being the second. We estimated, directly from the DES images, that the separation between them is ∼1.3 arcsec, which corresponds to roughly 2.5 binned pixels for our observing strategy. The 1D extracted spectra of the two components, source and lens, are shown in Fig. 4. where we also highlight the emission and absorption lines we used to infer the spectroscopic redshifts ($z_{s,WG2100} = 0.920 \pm 0.002$ and $z_{l,WG2100} = 0.203 \pm 0.002$).

Using the Penalized Pixel Fitting (PPXF) code of Cappellari (2017), we extracted the stellar velocity dispersion of the deflector from its absorption-line spectrum, using a maximum penalized likelihood approach. The spectrum has been extracted along an aperture of 3 pixels (corresponding to an aperture of roughly 1.5 arcsec), after subtracting the emission from the source (the broad MgII line at $\lambda \sim 5190$ Å observed wavelength). As stellar templates for the fit, we selected 100 stars (F, G, K, M) from the MILES stellar template library of Sánchez-Blázquez et al. (2006), which cover the wavelength range 3525–7500 Å at 2.5 Å FWHM spectral resolution. The resulting fit, yielding a $\sigma_\star = 287 \pm 40$ km s^{-1}, is shown in Fig. 5. The statistical uncertainty ($\delta\sigma_{stat} = 38$ km s^{-1}) and the systematic uncertainty ($\delta\sigma_{sys} = 14$ km s^{-1} due to the templates used, the region of the spectrum that we fitted, and the eighth order of multiplicative
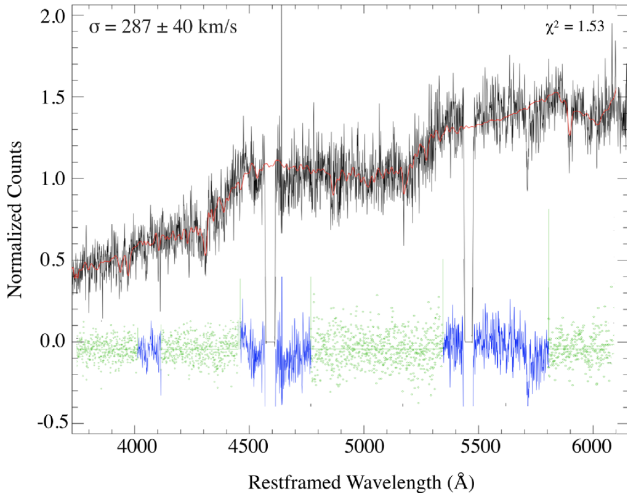
Figure 5. PPXF fit of the lens galaxy in WGA2100-4452 plotted in rest-frame wavelength and in normalized count units. The galaxy spectrum is showed in black and the best-fitting stellar template is overplotted in red. Residuals of the fit are shown in light green while blue regions are those excluded from the fit.

polynomial that we used to take care of the continuum) are added in quadrature.

6 LENS MODELS

To model the two quadruplets, we made use of the publicly available software GLAFIC, presented in Oguri (2010). The code allows one to efficiently fit lensed images for both point-like and extended sources, also handling multiple sources, and considering a wide range of lens potentials. We tested two different models to estimate the parameters: first, a singular isothermal ellipsoid (SIE) mass model, and second a power density ellipsoid (PDE) model where the mass density slope is left as free parameter. The SIE is one of the most frequently used lens model for strong gravitational lenses since it describes a mass distribution with a flat rotation curve. The convergence of the model is

$$\kappa = \frac{b_{SIE}(q)}{2\sqrt{\tilde{x}^2 + \tilde{y}^2/q^2}}, \tag{1}$$

where $q = 1 - e$ is the axial ratio (with e being the ellipticity), and the coordinates $\tilde{x}$, $\tilde{y}$ are rotated by the position angle PA_{SIE}, defined east of north and assuming that the positive direction is north. The normalization factor $b_{SIE}(q)$, for a spherical case ($q = 1$), agrees with the Einstein radius (θ_{SIE}) and is related to the galaxy velocity dispersion (σ_{SIE}) as:

$$b_{SIE}(q = 1) = \theta_{SIE} = 4\pi \left(\frac{\sigma_{SIE}}{c}\right)^2 \frac{D_{ls}}{D_s}, \tag{2}$$

where D_s is the angular diameter distance of the source from the observer and D_{ls} is the relative distance between the lens and the source.

The PDE model is more useful than the SIE model for studying the effect of the radial density slope on lensing. The convergence, defined in Keeton (2001), is

$$\kappa = \frac{3 - \beta}{2} (\theta_{PDE})^{1-\beta} \left(\tilde{x}^2 + \tilde{y}^2/q^2\right)^{(1-\beta)/2}, \tag{3}$$

where θ_{PDE} is the Einstein radius. The PDE model corresponds to an isothermal model for $\beta = 2$.

The SIE model has seven free parameters: x and y coordinates of the galaxy and of the source (true position), ellipticity, position angle, and velocity dispersion. The PDE has eight free parameters: Einstein radius, x and y coordinates of the galaxy and of the source, ellipticity, position angle, and mass density slope. Since from the DES images and photometric analysis we have eight constraints for each system (x, y, apparent positions of the four multiple images), both models are fully constrained.

We used the inferred spectroscopic redshifts for the sources ($z_{s,WG0214} = 3.229$, $z_{s,WG2100} = 0.92$). For the deflector redshifts, we used the spectroscopic value obtained for WG2100-4452 ($z_{l,WG2100} = 0.203$) and the photometric ones for WG0214-2105 (we run the model twice, one time assuming $z_{l_1,WG0214} = 0.22 \pm 0.09$, and the second time assuming $z_{l_2,WG0214} = 0.53 \pm 0.08$). The model results are reported in Table 4, where we also report reduced chi-square (χ_v^2) values to provide a quantitative measure of the goodness of the fit. Overall a good agreement between the two models is found. For the PDE model, the best fit mass density slopes we recovered are $\beta_{WG0214} = 2.1 \pm 0.2$ and $\beta_{WG2100} = 1.9 \pm 0.2$, both consistent with an isothermal profile.

For the SIE model, with the velocity dispersion derived by GLAFIC for each deflector redshift, we obtained and estimate of the Einstein radius from equation (2), and an estimate of the deflectors' masses inside the Einstein radii using the following equation:

$$M_{Ein} = \theta_{SIE}^2 \frac{c^2 D_l D_s}{4G D_{ls}}, \tag{4}$$

where D_l is the distance of the lens from the observer and c is the speed of light. Fig. 6 shows the mass models for WG0214-2105 (left-hand panel) and WG2100-4452 (right-hand panel) in the SIE case. We plot caustics and critical curves, as well as the apparent and true positions of the sources. We note that the flux ratios could be strongly perturbed by microlensing effects. Therefore, the magnitude difference of the quasar images has been excluded from the model.

Finally, we calculated the magnification and time-delay values for all components, relative to the brightest one (A), and report the results in Table 5 for both models. Unfortunately the code does not allow one to estimate the errors on time delays and magnitudes. We have therefore written a small python script to calculate them using a Markov-Chain Monte Carlo approach. We generated 100 000 models and obtained a normal distribution for each of the estimated parameters, computing, then, the mean and standard deviation values.

We caution the reader that microlensing can influence time-delay measurements, making them time variable. This is due, as described in Tie & Kochanek (2018), to a combination of two effects. First, the quasar disc has an inclination with respect to the line-of-sight, and thus different parts of the disc lie at different projected distances to the source. This configuration can change time delays on the scale of the light crossing time of the accretion disc (typically of the order of light days). Secondly, microlensing can cause a differential magnification of the temperature of the emission from the disc, causing a differential time delay on the scale of the light crossing time.

The results (expressed in changes of magnitudes and time delays with respect to the brightest component) obtained with the two different models agree with each other within 1σ errors. As expected, the SIE model produces smaller errors on all quantities, having less free parameters. Moreover, we note that the time delays highly depend on the deflector redshift: increasing the galaxy redshift, the time-delay values increase proportionally.

Table 4. Model parameters obtained for the two quadruplets: ellipticity, position angle, and Einstein radius from both models; mass density slope from PDE and galaxy velocity dispersion and masses within the Einstein radius from SIE. We also report, for each model and each system, the modest value of the χ^2 divided by the degrees of freedom to judge the quality of the fit. For WG0214-2105, we report model parameters obtained assuming $z_{l_1} = 0.22 \pm 0.09$ in the first line of the table, and assuming $z_{l_2} = 0.53 \pm 0.08$ in the second line of the table.

ID	$M(r < \theta_{SIE})$ $(10^{10}\,\mathrm{M_\odot})$	θ_{SIE} (arcmin)	θ_{PDE} (arcmin)	σ_{SIE} $(\mathrm{km\,s^{-1}})$	e_{SIE}	e_{PDE}	PA_{SIE} (°)	PA_{PDE} (°)	β_{PDE}	χ^2_ν SIE	χ^2_ν PDE
WG0214-2105 (z_{l_1})	6.1 ± 0.1	0.86 ± 0.02	0.90 ± 0.02	190 ± 2	0.3 ± 0.1	0.34 ± 0.16	62 ± 1	62 ± 1	2.1 ± 0.2	1.22	0.96
WG0214-2105 (z_{l_2})	12.8 ± 0.6	0.89 ± 0.02	0.91 ± 0.02	211 ± 2	0.3 ± 0.1	0.34 ± 0.16	62 ± 1	62 ± 1	2.1 ± 0.2	1.16	1.07
WG2100-4452	14.2 ± 0.4	1.30 ± 0.02	1.32 ± 0.03	251 ± 2	0.39 ± 0.05	0.34 ± 0.15	0.4 ± 0.7	0.6 ± 1.0	1.9 ± 0.2	1.08	0.96
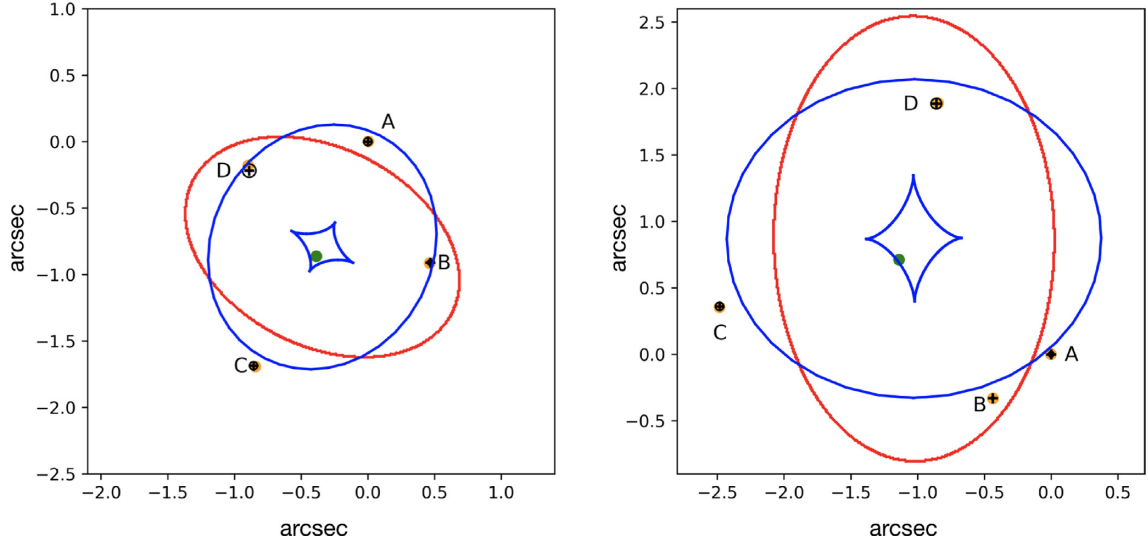
Figure 6. Mass model fit obtained assuming an SIE profile matter distribution for WG0214-2105 (left-hand panel) and WG2100-4452 (right-hand panel). The red and blue curves correspond to the critical curves and caustics of the model, respectively. The black circles with internal crosses show the observed positions inferred from the DES images, the orange filled circles show the predicted image positions, and finally the green filled circle indicates the calculated true source position for each system. The QSO components are labelled following the same convention adopted in Fig. 1.

Table 5. Quasar image parameters for the best fits obtained for the two models we tested: an SIE mass model and a PDE model. Component A is taken as reference. Since the time delays depend on the deflector redshift, for WG0214-2105, we provide time-delay values for both the fiducial photometric redshifts ($z_{l_1, WG0214} = 0.22 \pm 0.09$, $z_{l_2, WG0214} = 0.53 \pm 0.08$) separated by commas.

Name	Comp.	δx (arcmin)	δy (arcmin)	Δmag_{SIE} (mag)	Δmag_{PDE} (mag)	$\Delta t_{SIE, z_{l_1}}$ (d)	$\Delta t_{PDE, z_{l_1}}$ (d)	$\Delta t_{SIE, z_{l_2}}$	$\Delta t_{PDE, z_{l_2}}$
WG0214-2105	A	0.00 ± 0.02	0.00 ± 0.05	$\equiv 0$	$\equiv 0$	$\equiv 0$	$\equiv 0$	$\equiv 0$	$\equiv 0$
WG0214-2105	B	0.46 ± 0.05	-0.91 ± 0.01	0.7 ± 0.1	0.7 ± 0.2	0.8 ± 0.3	1.2 ± 0.8	3.5 ± 1.0	3.2 ± 1.6
WG0214-2105	C	-0.84 ± 0.04	-1.69 ± 0.05	0.7 ± 0.1	0.8 ± 0.2	-4.2 ± 1.5	-4.1 ± 3.3	-12.5 ± 2.9	-11.3 ± 7.3
WG0214-2105	D	-0.90 ± 0.06	-0.18 ± 0.04	0.6 ± 0.1	0.6 ± 0.1	1.2 ± 0.3	0.9 ± 0.5	2.5 ± 0.8	2.5 ± 1.6

Name	Comp.	δx (arcmin)	δy (arcmin)	Δmag_{SIE} (mag)	Δmag_{PDE} (mag)	Δt_{SIE} (d)	Δt_{PDE} (d)
WG2100-4452	A	0.00 ± 0.02	0.00 ± 0.01	$\equiv 0$	$\equiv 0$	$\equiv 0$	$\equiv 0$
WG2100-4452	B	-0.44 ± 0.01	-0.33 ± 0.01	0.12 ± 0.03	0.08 ± 0.12	0.15 ± 0.03	0.14 ± 0.08
WG2100-4452	C	-2.48 ± 0.03	0.35 ± 0.01	1.29 ± 0.05	-1.37 ± 0.13	-9.3 ± 1.6	-9.0 ± 4.3
WG2100-4452	D	-0.85 ± 0.02	1.89 ± 0.04	2.0 ± 0.1	-1.8 ± 0.2	11.8 ± 2.7	10.4 ± 4.0

The relative positions inferred from the lensing model and directly calculated from the images (in *r* band), always with respect to the brightest QSO component (A), agree perfectly with each other. This is also clearly visible from Fig. 6, where we report with orange filled circles the model predicted positions and with empty black circled crosses the positions directly obtained from the DES images.

7 CONCLUSIONS

In this paper, we have presented the spectroscopic confirmation and lens modelling of two new quadruply lensed quasars recently found in the DES public footprints, namely WG0214-2105 and WG2100-4452. The quadruplets were both found with a method based on three main steps: an infrared (WISE) colour-pre-selection

of QSO-like objects, a morphological criterion based on multiple matches in the *Gaia* DR2 catalogue and finally, visual inspection of the outcomes. We refer the reader to A18 and S18 for a detailed description of the search methodology and to A18 and ARN18 for the discovery reports.

Since the only missing ingredient to unambiguously confirm the lensing nature of these objects, whose geometrical configuration and chromaticity are typical of lensed QSOs, was spectroscopy, we targeted them with the Southern African Large Telescope. For both systems, we calculated the redshifts of the deflectors and the sources, confirming their multiple lensing nature. We obtained $z_s = 3.229 \pm 0.004$ for WG0214-2105 thanks to the identification of the strong Ly α line and other weaker lines such as Si IV, O IV], He II, O III]. We inferred instead $z_s = 0.920 \pm 0.002$ for WG2100-4452, thanks to the identification of the prominent Mg II emission line. Only for WG2100-4452 we could estimate the deflector redshift ($z_l = 0.203 \pm 0.002$) directly from the spectral absorption lines (i.e. CaK, CaH, G4300, H β, Mgb, NaD), since the galaxy is quite bright ($r = 17.68 \pm 0.01$ mag, see Table 2). For the other lens, we infer the redshift of the source using optical magnitudes that we obtained performing DIA and photometry (presented in Section 4).

Microlensing studies require multiple images of a system taken in different epochs. We presented here preliminary evidence of time variability for one of the two systems, WG0214-2105, obtained measuring the photometry of all the components from DES (taken in 2016) and Pan-STARRS (taken in 2014). A change of ≈ 0.4 mag is visible for the faintest QSO component (D), and other two components show smaller changes too. Although with only two epochs separated by 2 yr, intrinsic chromatic variability cannot be excluded, we argue in favour of microlensing because we do not see any clear correlation with wavelength. Moreover, the lens model inferred time delays are of the order of a few days and the probability that a quasar changes its magnitude by $\approx$ half a magnitude in such a short time is very low. We also note that, as shown in Schechter & Wambsganss (2002), microlensing in saddle-points (B, D) is more likely in the presence of a smoothly distributed (dark matter) component.

Finally, we confirmed the work of Wynne & Schechter (2018), finding that these systems are perfectly compatible with simple lens models. We tested two different lens models, specifically an SIE approximation where the mass density slope is fixed but the stellar velocity dispersion is allowed to vary, and a PDE model where the Einstein radius and the mass density slope are free parameters. For both models, we constrained the x and y positions of the source and the deflector, the ellipticity and the position angle. We finally obtained for both quadruplets changes in magnitudes and time-delay measurements for each of the quasar multiple image, finding that, overall, these quantities do not depend much on the chosen model.

To conclude, we demonstrated that the planned integration times (set by the magnitudes and colours of the sources in the photometric survey catalogues) are long enough to obtain SALT spectra with sufficient signal-to-noise ratios to detect emission lines from the QSOs and, in most of the cases, also absorption lines from the lens. Our observing strategy works properly and will allow us, once the programme will be completed, to confirm many among the $\sim$300 lens candidates (arcs and QSOs) that we selected in the last 2 yr from the KIDS and KABS surveys.

ACKNOWLEDGEMENTS

REFERENCES

Abbott T. M. C. et al., 2018, ApJS, 239, 18
Abolfathi B. et al., 2018, ApJS, 235, 42
Agnello A., 2018, RNAAS, 2, 42(ARN18)
Agnello A., Spiniello C., 2018, preprint (arXiv:1805.11103)(A18)
Agnello A. et al., 2017, MNRAS, 472, 4038
Blackburne J. A., Pooley D., Rappaport S., Schechter P. L., 2011, ApJ, 729, 34
Blandford R. D., Narayan R., 1992, ARA&A, 30, 311
Bonvin V. et al., 2017, MNRAS, 465, 4914
Buckley D. A. H., Swart G. P., Meiring J. G., 2006, in Stepp L. M., ed, Proc. SPIE Conf. Ser. Vol. 6267, Ground-based and Airborne Telescopes. SPIE, Bellingham, p. 62670Z
Capaccioli M., Schipani P., 2011, The Messenger, 146, 2
Cappellari M., 2017, MNRAS, 466, 798
Chambers K. C. et al., 2016, preprint (arXiv:1612.05560)
Courbin F. et al., 2018, A&A, 609, A71
Cowley M. J. et al., 2017, MNRAS, 473, 3710
Crawford S. M. et al., 2010, in Silva D. R., Peck A. B., Soifer B. T., eds, Proc. SPIE Conf. Ser. Vol. 7737, Observatory Operations: Strategies, Processes, and Systems III. SPIE, Bellingham, p. 773725
Dai X., Kochanek C. S., Chartas G., Koz lowski S., Morgan C. W., Garmire G., Agol E., 2010, ApJ, 709, 278
de Jong J. T. A. et al., 2015, A&A, 582, A62
de Jong J. T. A. et al., 2017, A&A, 604, A134
Eigenbrod A., Courbin F., Meylan G., Agol E., Anguita T., Schmidt R. W., Wambsganss J., 2008, A&A, 490, 933

Gaia Collaboration, 2016, A&A, 595, A2

Irwin M. J., Webster R. L., Hewett P. C., Corrigan R. T., Jedrzejewski R. I., 1989, AJ, 98, 1989

Keeton C. R., 2001, preprint (arXiv:astro-ph/0102340)

Kochanek C. S., 2004, ApJ, 605, 58

Kuijken K., 2011, The Messenger, 146, 8

Lee C.-H., 2019, AJ, 157, 14

Lindegren L. et al., 2016, A&A, 595, A4

Linder E. V., 2011, Phys. Rev. D, 84, 123529

Mediavilla E., Jiménez-Vicente J., Mu noz J. A., Vives-Arias H., Calderón-Infante J., 2017, ApJ, 836, L18

Morgan C. W., Kochanek C. S., Morgan N. D., Falco E. E., 2010, ApJ, 712, 1129

Oguri M., 2010, PASJ, 62, 1017

Oguri M., Marshall P. J., 2010, MNRAS, 405, 2579

O'Dowd M. J., Bate N. F., Webster R. L., Labrie K., Rogers J., 2015, ApJ, 813, 6

Palanque-Delabrouille N. et al., 2011, A&A, 530, A122

Peng C. Y., Ho L. C., Impey C. D., Rix H.-W., 2002, AJ, 124, 266

Petrillo C. E. et al., 2017, MNRAS, 472, 1129

Petrillo C. E. et al., 2019, MNRAS, 484, 3879

Refsdal S., 1964, MNRAS, 128, 307

Sánchez-Blázquez P. et al., 2006, MNRAS, 371, 703

Schechter P. L., Wambsganss J., 2002, ApJ, 580, 685

Schechter P. L., Wambsganss J., 2004, IAUS, 220, 103

Schmidt R. W., Wambsganss J., 2010, Gen. Relativ. Gravit., 42, 2127

Shanks T. et al., 2015, MNRAS, 451, 4238

Spiniello C. et al., 2018, MNRAS, 480, 1163(S18)

Suyu S. H. et al., 2012, preprint (arXiv:1202.4459)

Suyu S. H. et al., 2013, ApJ, 766, 70

Tie S. S., Kochanek C. S., 2018, MNRAS, 473, 80

Treu T., Marshall P. J., 2016, A&AR, 24, 11

Turner E. L., 1980, ApJ, 242, L135

Vernardos G., 2018, MNRAS, 480, 4675

Witt H. J., Mao S., Keeton C. R., 2000, ApJ, 544, 98

Wright E. L. et al., 2010, AJ, 140, 1868

Wynne R. A., Schechter P. L., 2018, preprint (arXiv:1808.06151)

[1]*INAF – Osservatorio Astronomico di Capodimonte, Salita Moiariello, 16, I-80131 Napoli, Italy*

[2]*European Southern Observatory, Karl-Schwarschild-Str 2, D-85748 Garching, Germany*

[3]*Astronomical Institute of Kharkov National University, 35 Sumskaya St, UA-61022 Kharkov, Ukraine*

[4]*Institute of Radio Astronomy of the National Academy of Sciences of Ukraine, 4 Mystetstv St., Kharkov, Ukraine*

[5]*Department of Astronomy, University of Cape Town, Private Bag X3, Rondebosch 7701, Cape Town, South Africa*

[6]*Department of Physics and Astronomy, University of the Western Cape, Private Bag X17, Bellville 7535, Cape Town, South Africa*

[7]*INAF – Istituto di Radioastronomia, via Gobetti 101, I-40129 Bologna, Italy*

[8]*INAF – Osservatorio Astrofisico di Arcetri, Largo Enrico Fermi 5, I-50125 Firenze, Italy*

[9]*School of Physics and Astronomy, Sun Yat-Sen University Zhuhai Campus, 2 Daxue Road, Tangjia, Zhuhai, Guangdong 519082, P.R. China*

[10]*O. Ya. Usikov Institute for Radiophysics and Electronics, National Academy of Sciences of Ukraine, 12 Ac. Proskura St., UA-61085 Kharkov, Ukraine*

[11]*Departamento de Física Moderna, Universidad de Cantabria, Avda. de Los Castros s/n, E-39005 Santander, Spain*

[12]*DARK, Niels Bohr Institute, Copenhagen University, Lyngbyvej 2, DK-2100 Copenhagen, Denmark*

[13]*School of Physical Sciences, The Open University, Milton Keynes MK7 6AA, UK*

[14]*Kapteyn Astronomical Institute, University of Groningen, PO Box 800, NL-9700 AV Groningen, the Netherlands*

[15]*Rutgers, The State University of New Jersey, Department of Physics and Astronomy, 136 Frelinghuysen Road, Piscataway, NJ 08854-8019, USA*

[16]*Dipartimento di Fisica 'E. Pancini', Universitá di Napoli Federico II, Compl. Univ. Monte S. Angelo, I-80126 Napoli, Italy*

[17]*INFN, Sezione di Napoli, Compl. Univ. Monte S. Angelo, I-80126 Napoli, Italy*

This paper has been typeset from a TEX/LATEX file prepared by the author.